RSC Advances

PAPER

View Article Online
View Journal | View Issue

Cite this: *RSC Adv.*, 2023, **13**, 34660

Tailoring carboxylatopillar[5]arene-modified magnetic graphene oxide nanocomposites for the efficient removal of cationic dyes†

Yu Huang,‡[a] Yanqin Rong,‡[a] Wenjia Zhang,[a] Zibin Zhang, *[b] Xiaoyuan Zhang,[a] Wenting Liang *[a] and Cheng Yang *[ac]

A carboxylatopillar[5]arene-embellished (CP5) magnetic graphene oxide nanocomposite (MGO@CP5) was smoothly constructed *via* a mild layer-by-layer method. The morphology, structure, and surface characteristics of this nanocomposite was investigated by field-emission scanning electron microscopy, transmission electron microscopy, Fourier transform infrared spectroscopy, Raman spectroscopy, zeta potential, and other techniques. Benefiting from a high capture ability for small molecules of CP5 as a supramolecular host molecule, along with a negative surface charge and large surface area of MGO@CP5, this nanocomposite exhibits an ultrafast, efficient adsorption property for representative cationic dyes: methylene blue (MB) and basic fuchsin (BF). The removal efficiency of MB and BF can reach nearly 99% within 3 min, while the maximum adsorption capacity of the two dyes reaches 240 mg g^{-1} for MB and 132 mg g^{-1} for BF. Furthermore, owing to excellent magnetic responsiveness from the tight loading of Fe_3O_4 nanoparticles on graphene oxide, MGO@CP5 could be easily and magnetically separated, regenerated, and reused four times without an evident reduction in the removal efficiency (>95%). Impressively, the adsorption property of MGO@CP5 reveals a strong tolerance to pH changes and ionic strength interference, which renders it a promising adsorbent in the field of water treatment.

Received 19th October 2023
Accepted 9th November 2023

DOI: 10.1039/d3ra07124c

rsc.li/rsc-advances

Introduction

With the rapid development of urbanization and industrialization, dyes have been extensively used in various industries, such as printing, textile, food, and plastic industries. Dyes are known to play an exceedingly crucial role in bolstering economic progress and enhancing the quality of life for individuals. However, dye abuse inevitably engenders deleterious consequences on ecosystems by virtue of its inherent toxicity, non-biodegradability, and bioaccumulation, thereby posing a grave threat to the availability of freshwater resources, aquatic biodiversity, and human health.[1–4] Hence, it is of paramount importance to explore an environmentally sustainable, facile, and cost-effective approach for the remediation and treatment of dyes. To date, from the perspective of environmental protection and sustainable development, various treatment methods, including chemical oxidation,[5] biodegradation,[6] photodegradation,[7] membrane filtration,[8] and adsorption,[9] have been devised for eliminating dyes from water. Among these advanced treatment strategies, the adsorption technique is particularly appealing owing to its cost-effectiveness, simplicity, easy operation, and a high removal efficiency.[10,11] At present, traditional adsorbents like activated carbon, zeolite, and resins have been frequently utilized as commercial products for wastewater treatment.[12,13] Unfortunately, several constraints have been imposed on the rapid and plentiful adsorption capacity for dye pollutants owing to insufficient interaction sites for dye molecules. Furthermore, non-ecofriendly preparation process, hard separation, and difficult regeneration also have limited their applications. As a result, there exists an urgent necessity to introduce a prospective adsorbent for conspicuously enhancing the adsorption rate and capability.

It is acknowledged that graphene oxide (GO) and graphene with a two-dimensional (2D) conjugated plane structure exhibit unusual physicochemical properties, including high carrier mobility and high mechanical strength. These arouse great interests in the field of both theoretical research and practical

[a]*Institute of Environmental Science, School of Chemistry and Chemical Engineering, Shanxi University, Taiyuan, 030006, China. E-mail: liangwt@sxu.edu.cn*

[b]*College of Material, Chemistry and Chemical Engineering, Key Laboratory of Organosilicon Chemistry and Material Technology, Ministry of Education, Key Laboratory of Organosilicon Material Technology, Hangzhou Normal University, Hangzhou 311121, China. E-mail: zzhang@hznu.edu.cn*

[c]*Key Laboratory of Green Chemistry & Technology of Ministry of Education, Sichuan University, Chengdu 610064, China. E-mail: yangchengyc@scu.edu.cn*

† Electronic supplementary information (ESI) available: ^{1}H NMR and ^{13}C NMR spectrum of CP5; EDS analysis of MGO and MGO@CP5; XRD pattern and N_2 adsorption/desorption isotherm and corresponding parameters of MGO@CP5; the standard curves of BF and MB; the structure of MO, BF and MB; UV-vis adsorption spectra and color change images before and after adsorption of MO, BF and MB; comparison of adsorption capacities toward MB and BF with various adsorbents. See DOI: https://doi.org/10.1039/d3ra07124c

‡ The authors contributed equally: Yu Huang, Yanqin Rong.

applications.[14–22] Especially, by virtue of the facile post-functionalization feature, inherent high specific surface area, and abundant substrate adsorption sites, GO has generally been regarded as a kind of promising absorbent, attracting significant attention for its potential use in effluent treatment. Despite these beneficial aspects, GO-based adsorbents frequently suffer from the drawbacks of easy aggregation and low adsorption capacity. Impressively, Fe_3O_4 magnetic nanoparticles (MNPs) reveal favorable magnetic properties, considerable catalytic ability, long reusability, and environment-friendly effect. Currently, MNPs have commonly been selected as a functional block to improve the dispersibility and stability of GO-based nanomaterials. The synergistic combination of MNPs and GO yields an outstanding adsorption–separation performance, providing an innovative solution for water purification endeavors.[23–26] Nevertheless, the as-obtained MNPs-decorated GO (MGO) tends to exhibit the limited adsorption capacity. Thus, further surface modifications of MGO with diverse functional molecules are crucial to promote adsorption behaviors.[27,28] Pillar[*n*]arenes and their derivatives represent a new category of macrocyclic compounds composed of *n* hydroquinone units held together by methylene bridges ($-CH_2$), which are well-known as ideal modifiers for possessing unique pillar-shaped architectures with well-defined hollow space and rigid π-rich cavities.[29–31] In light of these distinctive attributes, pillar[*n*]arenes have demonstrated a notable propensity to interact strongly with dyes or organic pollutants, making them the host molecules with considerable interests and promising applications in the field of wastewater treatment.[31–34] Consequently, pillar[*n*]arenes and MGO-conjugated nanomaterials may be served as desirable adsorbents, achieving the effective treatment of dyes through the synergistic action of these three components.

Herein, our work focused on the rational design of a new kind of adsorbent, namely, carboxylatopillar[5]arene (CP5)-modified magnetic graphene oxide (MGO@CP5) nanocomposite, which was constructed by a mild layer-by-layer method (Scheme 1). In this regard, GO acted as both a carrier and raw material. Initially, Fe_3O_4 MNPs were successfully fabricated *via* chemical precipitation and smoothly loaded onto the surface of GO to give the MGO. However, the currently direct reaction between MGO and CP5 was difficult and challenging. To address this, further modifications of MGO to introduce amino groups were carried out, bringing about the synthesis of amino-MGO. Subsequently, amino-MGO could react with carboxyl-derived CP5 by the amide condensation method to obtain the MGO@CP5 nanocomposite. Finally, based on the supramolecular recognition strategy, we explored the practical applicability of MGO@CP5 for removing representative cationic dye pollutants including methylene blue (MB) and basic fuchsin (BF) in water. As expected, the proposed MGO@CP5 adsorbent perfectly unified the charming merits of high adsorption from GO-based nanomaterials, facile separation performances of MNPs, and considerable host–guest interaction of CP5 toward dyes, which was confirmed to exhibit the high adsorption efficiency for MB and BF removal. The adsorption kinetic and isotherm progress toward dye models, influence of pH and ionic strength, and external magnetic field-controlled recycling experiment were also systematically evaluated. Moreover, MGO@CP5 revealed the selective removal potential toward MB and BF in mixed dye systems. With respect to the above facts, we anticipate that this MGO@CP5 adsorbent would be extensively applicable to the elimination of a diverse array of other emerging cationic dye pollutants.

Experimental section

Materials and instruments

Graphite powder and ferric chloride hexahydrate ($FeCl_3 \cdot 6H_2O$), ferrous chloride tetrahydrate ($FeCl_2 \cdot 4H_2O$), basic fuchsin (BF), methylene blue (MB), and ammonia solution (NH_3, 25%) were purchased from Macklin Biochemical Co., Ltd, Shanghai. 1-

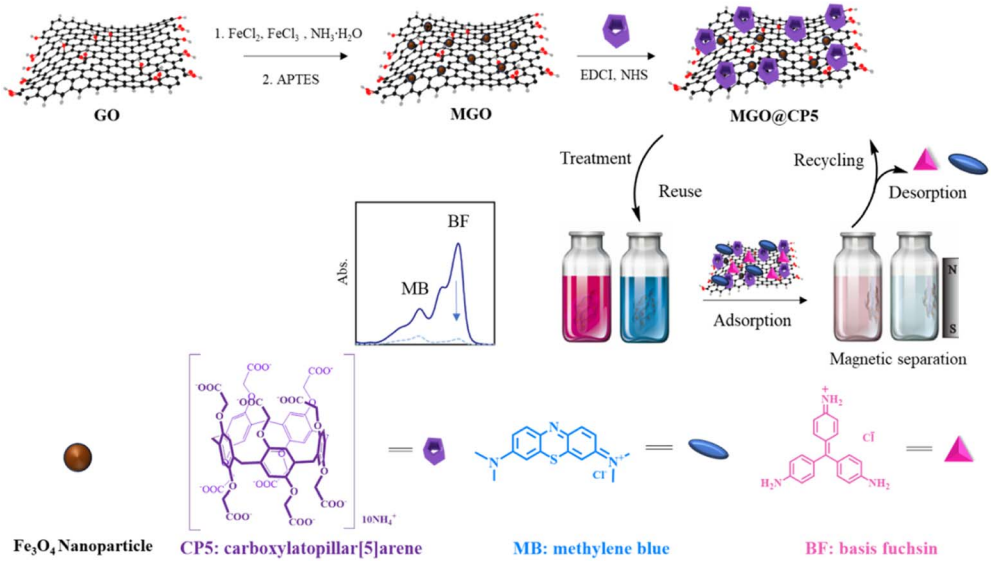

Scheme 1 A schematic diagram for the synthesis of MGO@CP5 and adsorption of MB and BF on MGO@CP5.

Ethyl-3-(3-dimethylaminopropyl)carbodiimide (EDCI), *N*-hydroxysuccinimide (NHS), and 3-aminopropyl triethoxysilane (APTES) were all provided by Shanghai Aladdin Industrial Corporation. All such available chemicals were of analytical grade from local suppliers and used without further purification. Ultra-pure water was purified with a Millipore system (Millipore, Burlington, MA, USA) throughout the whole experiment.

The size and morphology of the nanoparticles were observed on a Mira3 LMH (Tescan, China) by scanning electron microscopy (SEM) and a JEM-2100F (JEOL) by transmission electron microscopy (TEM) with energy-dispersive X-ray spectrometry (EDS). Fourier transform infrared spectroscopy (FT-IR) analysis was undertaken with a Bruker Tensor 27 (Ettlingen, Germany), using KBr as the background in the range from 4000 cm^{-1} to 500 cm^{-1}. Raman spectroscopy was performed on a Horiba 800. Thermogravimetric analyses (TGA) were carried out on a TA Instruments Q50 (New Castle, DE, USA). The samples were heated from ambient temperature to 800 °C at a heating rate of 10 °C min^{-1} under a flowing nitrogen atmosphere (40 mL min^{-1}). A zeta potential instrument (Malvern Instrument, UK) was applied to record the electrical properties on the surface of the adsorbent at 25 °C with the initial solution pH ranging from 3 to 10. The NMR spectra were obtained by a Bruker NMR spectrometer (AVANCE III HD-600 MHz). The powder X-ray diffraction (PXRD) pattern was collected using a Germany Bruker D8 advance diffractometer, operating at 40 kV and 40 mA with Cu Kα radiation (λ = 0.15406 nm). N_2 adsorption/desorption analysis was done on a Beishide Instrument (BSD-660S A6) to investigate the Brunauer–Emmett–Teller (BET) surface areas and pore size distribution.

Fabrication of MGO@CP5

Graphene oxide (GO) was prepared by the Hummers' method from natural graphite powder according to previously reported literature,[35,36] while amino-MGO was synthesized following our previous work.[16,17] The specific process was as follows: firstly, the prepared MGO (40 mg) were dispersed completely in ethanol (40 mL, 99.5%) for 0.5 h under the ultrasonic condition, followed by the addition of 60 μL APTES under a nitrogen atmosphere; subsequently, the obtained mixed solution was stirred by mechanical agitation for 4 h at 45 °C; after cooling to room temperature, this resulting material was washed with ethanol and ultra-pure water three times, then separated by a permanent magnet and finally freeze-dried for a whole day to yield amino-MGO.

The MGO@CP5 composite was fabricated through an amide condensation reaction between carboxyl-derived CP5 and MGO mixed with EDCI–NHS activating agents. In detail, carboxylatopillar[5]arene (CP5) was acquired as per previous reports,[37,38] and its structure was verified by ^{1}H NMR and ^{13}C NMR spectra, as depicted in Fig. S1 and S2.† In order to obtain activated CP5, CP5 (30 mg) was firstly dissolved in ultra-pure water (30 mL) for the formation of a homogeneous dispersion, then the EDCI–NHS system (EDCI: 27.46 mg; NHS: 16.47 mg) was sequentially introduced into the above aqueous solution with continuous stirring for 1 h at room temperature. Afterward, amino-MGO (30 mg) was added into the mixture and stirred for another 24 h at room temperature to ensure the reaction completely. The resulting material was separated using an external magnet and washed with ethanol and ultra-pure water repeatedly. Ultimately, MGO@CP5 powder was achieved after lyophilization.

Adsorption and desorption studies

Synthetic wastewater of BF or MB in a single system was respectively obtained by dissolving solid dyes in ultra-pure water. For the actual experimental procedure, the stock solution of BF or MB (20 mg mL^{-1}) was prepared beforehand, and the working solutions were prepared by diluting the stock solution to a specified multiple according to experimental requirements. Adsorption tests throughout the entire process were performed on a shaker at room temperature with a shaking speed of 200 rpm and underwent several repetitions at 25 °C.

The adsorption kinetic experiments were conducted by the analysis of sampled solutions at certain time intervals, guaranteeing that the concentration of BF and MB was 2 mg L^{-1} (5 μM) and 3.2 mg L^{-1} (0.01 mM), respectively. As for the adsorption isotherm experiments, a series of concentrations ranging from 0.01 mM to 1 mM (3.2 g L^{-1} to 320 g L^{-1}) were investigated. In the pH and ionic strength influence measurements, the pH levels and ionic strength were adjusted to the required values by HCl (0.01 M)/NaOH (0.01 M) solution and solid NaCl, respectively. In the above process, the reaction time was kept for 3 h to ensure the achievement of adsorption equilibrium.

After adsorption, sample materials were gathered by magnetic separation. The initial and residual concentrations of dye solution were calculated with a standard curve between concentration and absorbance (Abs.) measured by a UV-vis spectrophotometer (Lambda 950, PerkinElmer). The dye removal efficiency (R, %), the adsorption amounts at different time intervals (q_t, mg g^{-1}), and equilibrium adsorption capacities (q_e, mg g^{-1}) were calculated by eqn (1)–(3), respectively.

$$R\ (\%) = \frac{\rho_0 - \rho_e}{\rho_0} \times 100\% \quad (1)$$

$$q_t = (\rho_0 - \rho_t)\frac{V}{m} \quad (2)$$

$$q_e = (\rho_0 - \rho_e)\frac{V}{m} \quad (3)$$

where ρ_0 (mg L^{-1}) is the initial concentration, ρ_t (mg L^{-1}) and ρ_e (mg L^{-1}) are concentration at time t and equilibrium concentration of BF and MB, respectively, V (mL) is the solution volume, and m (mg) is the mass of MGO@CP5.

Reusability tests

The reusability of MGO@CP5 toward BF and MB was evaluated by desorption and re-adsorption capability, respectively. The desorption process was performed by adding the materials

adsorbed BF and MB into EtOH containing 0.01 M HCl (the volume ratio is $V_{EtOH} : V_{HCl} = 8 : 1$) for 1 h under the condition of ultrasonication to promote the desorption of dye molecules. MGO@CP5 was regained through separation by a permanent magnet. After vacuum-drying at 45 °C, the next adsorption study was conducted using the regained MGO@CP5. The recycling studies were ultimately carried out five times as per the above methods.

Results and discussion

Characterization of MGO@CP5

The microstructure and surface morphology of both MGO and MGO@CP5 were characterized by SEM and TEM. As can be seen from Fig. 1a, the SEM image of MGO presented a typical layered structure of graphene-based materials. For MGO@CP5, despite its similar layered architecture to that of MGO, the surface of MGO@CP5 appeared to be rougher (Fig. 1b). This possibly resulted from the attachment of some irregular materials, indicating that MGO was smoothly modified with CP5. Concurrently, the evidence of the presence of Fe_3O_4 particles in MGO and MGO@CP5 was provided by EDS analysis (Fig. S3†), which demonstrated that Fe element existed in the composition of MGO and MGO@CP5. In the inset of Fig. 1b, MGO@CP5 originally dispersed in the solution was attached rapidly and tightly to the side, approaching an external magnet, further evidencing the magnetic property of MGO@CP5. The morphology and size distribution of MGO@CP5 was further analyzed by TEM. As displayed in Fig. 1c, Fe_3O_4 magnetic nanoparticles (Fe_3O_4 MNPs) were uniformly distributed on the surface of GO with an average particle size of 11 nm (the inset of Fig. 1c). The high-resolution TEM (HRTEM) image further revealed a distinct lattice structure of Fe_3O_4 MNPs on the MGO, with a lattice spacing of 0.25 nm corresponding to the Fe_3O_4 (311) crystal plane (Fig. 1d).[17] The XRD diffraction pattern of MGO@CP5 also exhibited all diffraction peaks of Fe_3O_4 (Fig. S4†), proving that modification with CP5 does not affect the crystal feature of Fe_3O_4 on MGO.

To identify the chemical bonds and functional groups in the as-prepared materials, the FT-IR spectra of MGO, CP5, MGO–APTES, and MGO@CP5 are shown in Fig. 2a. For the spectra of MGO, the intense and broad peak at about 3426 cm^{-1} belonged to the –OH stretching vibration, and the band at 585 cm^{-1} was attributed to the Fe–O bond in the Fe_3O_4 nanoparticles. The bands at 3059 cm^{-1} and 2915 cm^{-1} in the spectra of CP5 were respectively assigned to the aromatic C–H stretches and $-CH_2$ stretches connected to the benzene ring, and the signal at 1504 cm^{-1} was due to the stretching vibration of aromatic C=C for CP5. The stretching vibration of C–O–C was located at 1208 cm^{-1} and 1084 cm^{-1}. Meanwhile, the peak at 1736 cm^{-1} was assigned to the stretching vibration of C=O. As regards MGO@CP5, the corresponding peaks of main groups in MGO and CP5 were also all shown in its spectrum. These phenomena demonstrated the successful functionalization of CP5 on the surface of magnetic MGO.

The thermal stability of the resulting MGO, CP5, and MGO@CP5 were also characterized by TGA, as shown in Fig. 2b. Obviously, there existed a similar weight loss stage in the temperature region of 25–120 °C in the curves of three materials, which was caused by the evaporation of physically absorbed water. For the MGO sample, a minor loss in weight was observed from 25 °C to 800 °C, indicating that MGO possessed good thermal stability in the whole temperature period, whereas CP5 started to decrease the weight at approximately 120 °C, which subsequently underwent two remarkable weight

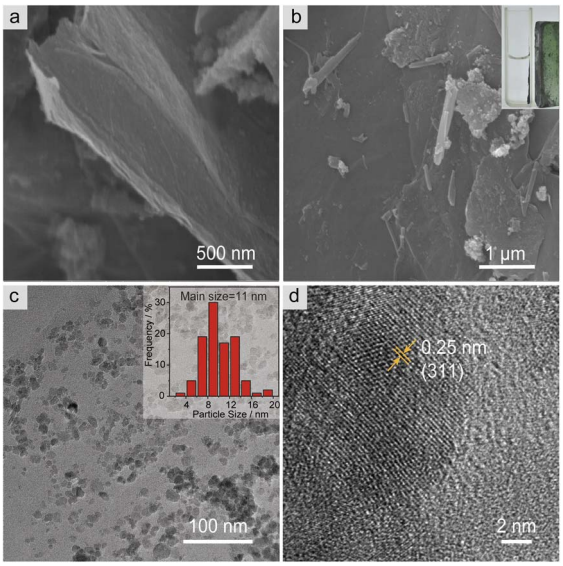

Fig. 1 The SEM images of MGO (a) and MGO@CP5 (b); the inset shows the picture of MGO@CP5 solution with an external magnet. (c and d) The TEM images of MGO@CP5; the inset shows the particle size distribution of Fe_3O_4 in MGO@CP5 from TEM.

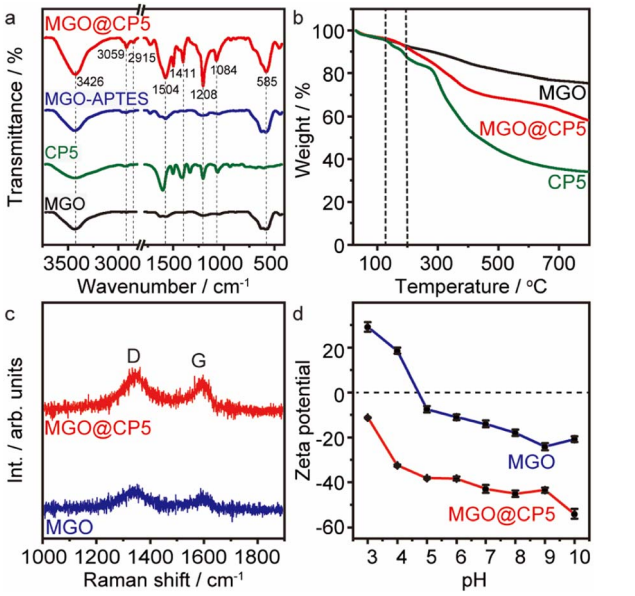

Fig. 2 (a) The FT-IR spectra of MGO, CP5, MGO–APTES, and MGO@CP5; (b) TGA curves of MGO, CP5, and MGO@CP5; (c) Raman spectra of MGO and MGO@CP5; and (d) zeta potential of MGO and MGO@CP5 with different pH values.

losses in the curve. The loss was visible between 120 °C and 270 °C, possibly attributed to the removal of labile oxygen-containing functional groups on CP5. Then, CP5 further drastically lost weight over 270 °C, which was related to the decomposition of the CP5 skeleton. In contrast, the significant weight reduction for MGO@CP5 appeared until the temperature rose to 200 °C, which exceeded the value to start the decomposition of CP5 (120 °C) under the same conditions. This suggested that MGO@CP5 enhanced the thermal stability relative to CP5 due to the deposition of CP5 on MGO. Afterward, despite a similar weight loss trend of MGO@CP5 as that of CP5 in the range of 200–650 °C, a relatively large weight loss was observed for MGO@CP5 than CP5 at a high temperature (650–800 °C), which might be assigned to the breakdown of the silane group in the inner layer and the polymer backbone from APTES. These led to the final residual weights to be 58 wt% of their original ones for MGO@CP5. Overall, the improved thermal stability of MGO@CP5 could potentially extend its application possibilities as an absorbent.

Raman spectroscopy was further applied to investigate the structural properties of MGO and MGO@CP5, as illustrated in Fig. 2c. The intensity ratio of the D-band to the G-band (I_D/I_G) is frequently used to express the degree of defects and disorders of carbon materials. The I_D/I_G ratio was calculated to be 1.03 for MGO. Compared with MGO, the decreasing I_D/I_G (1.02) value of MGO@CP5 suggested the partial disappearance of defects and the increasing graphitization degree on the surface of MGO after the modification of CP5.[39] The specific surface area was another extremely important parameter for evaluating the function of adsorbents. The specific surface area, pore volume, and average pore size of MGO@CP5 were calculated by the BET method and BJH analysis, and the results are revealed in Fig. S5 and Table S1.† The surface area, total pore volume, and average pore size of MGO@CP5 were 128.3 $m^2\ g^{-1}$, 0.35 $m^3\ g^{-1}$, and 4.03 nm, respectively. It was worth noting that the great surface area for MGO@CP5 was probably explained by the synergistic effects from the large specific surface area of MGO and the effective loading of CP5. For this reason, MGO@CP5 could be considered as a promising and superior adsorbent in the adsorption application.

The pH value of the solution affects the surface charge and the dissociation of functional groups on the active site of the adsorbent. Accordingly, the zeta potentials of MGO and MGO@CP5 in aqueous solution were obtained with different pH values at 298 K (Fig. 2d). It was explicit that the zeta potentials of MGO@CP5 showed more negative values by comparison with MGO and almost achieved a decrease with increasing pH. Even, there was no appearance of the zero-point charge on MGO@CP5. It further proved that MGO@CP5 was negatively charged in the whole pH range of 3–10, which is conductive to the adsorption of cationic dyes.

Dye adsorption studies

To evaluate the removal performance of MGO@CP5 toward dyes in an aqueous solution, adsorption experiments were performed applying cationic dyes including basic fuchsin (BF, Fig. 3a) and methylene blue (MB, Fig. 3b) as the analytes. As can be seen from Fig. 3, after the adsorption of BF and MB by MGO@CP5, the absorbance value for BF at 540 nm and for MB at 668 nm experienced a greater decrease than that of MGO. Meanwhile, BF (pink) and MB (blue) solutions turned almost colorless other than MGO, indicating that MGO@CP5 was more effective than MGO in the removal of BF (Fig. 3a) and MB (Fig. 3b). Thus, CP5-modified MGO nanocomposite (MGO@CP5), as a kind of new-type adsorbing material in the dye removal system, was potentially adopted in the treatment of wastewater containing BF or/and MB *via* the excellent traits of two components. Additionally, before conducting systematic adsorption studies, the standard curves of two model dyes were acquired by UV-vis spectra measurements in advance, and detailed points are shown in Fig. S6.†

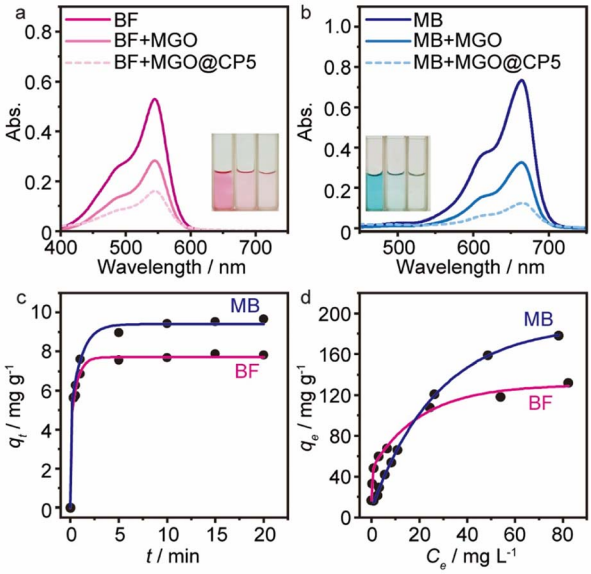

Fig. 3 (a and b) The UV-vis spectra of BF (0.01 mM) and MB (0.01 mM) before and after adsorption by MGO (1 mg) and MGO@CP5 (1 mg); inset shows the photographs of BF and MB dye before (left) and after the uptake by MGO (middle) or MGO@CP5 (right). (c) The adsorption kinetics of MGO@CP5 for BF and MB removal. (d) The adsorption isotherms of MGO@CP5 for BF and MB removal at room temperature.

Adsorption kinetics

The time dependence of BF and MB adsorbed onto MGO@CP5 was investigated to better understand the adsorption process. As depicted in Fig. 3c, it was found that a relatively rapid dye adsorption process occurred after the addition of the MGO@CP5 within the first 3 minutes, followed by a mild slowing adsorption rate, leading to the achievement of equilibration at 15 minutes. No significant increase in the adsorption capacity was noticed after the contact time exceeded 15 minutes. Among the above facts, in the initial stage of the adsorption process, the rapid and large increase of q_t was maybe due to the higher dye concentration gradient and more available sites on the surface of the MGO@CP5. Subsequent small increments in the adsorption amount could be given the credit

to the lower dye concentration and the reduced available active sites on the adsorbent surface as a result of the occupation in the adsorption process of initial time.

For the purpose of analyzing the adsorption kinetics more accurately, the kinetic data were generally analyzed by four kinetic models including pseudo-first-order (PFO), pseudo-second-order (PSO), and Elovich and Weber's intraparticle diffusion models, as expressed in eqn (4)–(7).

$$\ln(q_e - q_t) = \ln q_e - k_1 t \quad (4)$$

$$\frac{t}{q_t} = \frac{1}{k_2 {q_e}^2} + \frac{t}{q_e} \quad (5)$$

$$q_t = \beta \ln(\alpha\beta) + \beta \ln(t) \quad (6)$$

$$q_t = k_p t^{0.5} + C \quad (7)$$

where q_e (mg g^{-1}) and q_t (mg g^{-1}) stand for the adsorption capacity of the adsorbent at equilibrium and time t (min); k_1 (min^{-1}) and k_2 (g mg^{-1} min^{-1}) are the rate constant of PFO and PSO, respectively; the α (mg g^{-1} min^{-1}) value is the initial sorption rate, the β value (g mg^{-1}) value is the coverage degree of surface sites; k_p (mg g^{-1} min^{-1}) represents the rate constant of the intraparticle diffusion model; C (mg g^{-1}) is the constant that varies directly with the adsorption step.

The fitted curves of these models and obtained kinetic parameters are presented in Fig. 4a–d and Table S2,† respectively. Notably, for the first three models, the PSO model was well-fitted to describe the adsorption process of BF and MB due to the larger regression coefficients ($R^2 > 0.99$) than the PFO and Elovich model. As is well known to all, the PSO assumed that the adsorption rate was controlled by chemical sorption; at the same time, the adsorption ability was proportional to the number of active sites on the MGO@CP5. The intraparticle diffusion model was also assessed to further figure out the rate-limiting steps and the diffusion mechanism. As displayed in Fig. 4d and Table S2,† for two kinds of dyes, it was evident for three linear regions in the multi-linear plot of q_t *versus* $t^{0.5}$, suggesting that there were three phases in the whole adsorption process of MB or BF. In the first stage, the organic dye molecules were quickly transported from the liquid phase to the surface of MGO@CP5 by film or surface diffusion, which was accompanied by the strongest mass transfer driving force and the highest adsorption rate. Once most of the active sites on the surface of MGO@CP5 were occupied, the next stage began; thus, the dye molecules started to diffuse from the surface into the pores *via* intraparticle diffusion and were even adsorbed in the interior position. Ultimately, the adsorption rate sharply decreased until it achieved the equilibrium. We attribute this to the decrease in the obtainable active sites and residual content of dyes at the third stage of equilibrium one. In addition, from different nonzero y-intercepts and R^2 in the plots of three levels, it could confirm that the adsorption process was not only controlled by intraparticle diffusion but involved a complex mechanism pathway.

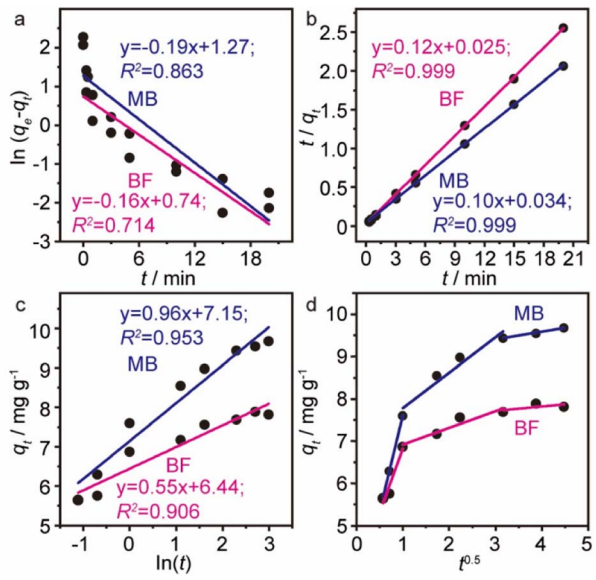

Fig. 4 The fitting of adsorption kinetic data with pseudo-first-order (a), pseudo-second-order (b), Elovich (c), and intraparticle diffusion models (d) for BF and MB of MGO@CP5.

Adsorption isotherms

With the intention to evaluate the BF and MB uptake capacity by MGO@CP5, adsorption isotherm measurements were conducted at 298 K with various initial concentration (C_0) of two dyes ranging from 0.01 mM to 1 mM. As illustrated in Fig. 3d, the adsorption uptakes increased with the gradually elevated initial concentrations for BF and MB and reached an equilibrium state at an initial concentration of 1 mM, giving the highest capture capacity of 120 mg g^{-1} (BF) and 180 mg g^{-1} (MB). The increasing dye concentration was the significant driving force in overcoming the mass transfer resistance of dye molecules between the solid and aqueous phases. Furthermore, three typical adsorption isothermal model including Langmuir, Freundlich, and Temkin were typically employed to deeply depict the adsorption isotherm data, and their non-linear forms were expressed by the following eqn (8)–(10).

$$\frac{C_e}{q_e} = \frac{1}{K_L q_m} + \frac{C_e}{q_m} \quad (8)$$

$$\ln q_e = \frac{1}{n} \ln C_e + \ln K_F \quad (9)$$

$$q_e = a \ln K_T + a \ln C_e \quad (10)$$

where C_e (mg L^{-1}) represents the concentration at equilibrium; q_e (mg g^{-1}) was the amount of adsorbed dyes at the equilibrium; q_m (mg g^{-1}) was the maximum capacity; K_L (L mg^{-1}), K_F (mg g^{-1}), and K_T (Lg^{-1}) are the Langmuir, Freundlich, and Temkin isothermal constant, respectively.

The results of isothermal fitting are displayed in Fig. 5a–c, and the corresponding parameters are shown in Table S3.† It was apparent that the correlation coefficients R^2 of fitting linear curves for the Langmuir model was the highest in all the

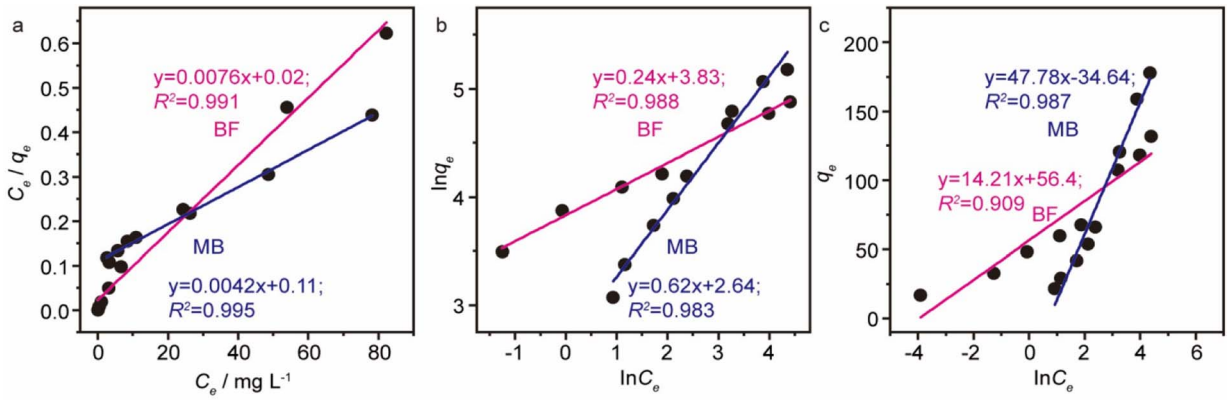

Fig. 5 The fitting of adsorption isotherm data with Langmuir (a), Freundlich (b), and Temkin (c) models for BF and MB of MGO@CP5.

models. This meant that the Langmuir model was more suitable for understanding the adsorption behaviour of BF and MB onto MGO@CP5, which inferred that the adsorption process belonged to the homogeneous monolayer adsorption. According to the Langmuir model fitted isotherm data, it could be calculated that the maximum uptake capacities of MGO@CP5 toward BF and MB were 132 mg g^{-1} and 240 mg g^{-1}, respectively, presenting good consistencies with the above adsorption amounts obtained by experiments. Further, compared to the other reports on the capture of BF and MB in Table S4,† the high adsorption amount of MGO@CP5 might originate from the large specific surface area brought by the unique structure of MGO with the immobilization of CP5, displaying the superiority for the practical removal of two dyes.

Influence of pH and ion strength

Undeniably, the pH value of the solution is a pivotal factor for adsorption, which can affect the surface charge and ionization extent of both the model dyes (BF, MB) and MGO@CP5. As mentioned in Fig. 2d, all the zeta potential values of MGO@CP5 were negative without an isoelectric point and with a stepwise decrease when the pH values increased, *i.e.*, MGO@CP5 tended to trap cationic dyes in water through electrostatic interaction. In fact, as shown in Fig. 6a, the removal efficiencies of MGO@CP5 toward BF and MB (>90%) in different pH ranges from 3 to 10 were also measured to be stable with no significant dependence on the pH values. The possible reason was that more –COO– and –O– groups content on the surface of MGO@CP5 could produce more negative charges, leading to the preference to adsorb the cation dyes with a positive charge in its structure. In other words, cationic dyes tended to be electrostatically attracted to the carboxyl and hydroxyl groups in MGO@CP5. The above phenomena implied that electrostatic interaction might make a vital difference in the adsorption of cationic dye molecules by MGO@CP5.

For the sake of ascertaining the effect of ionic strength on the adsorption behavior, the ionic strength of the solution was changed by adjusting different concentration of NaCl from 0 to 2 mol L^{-1}. From Fig. 6b, a significant variation in the removal rate for independent MB or BF removal in the whole range of 0–2 mol L^{-1} for NaCl was absent, proving that the adsorption behavior of MGO@CP5 for MB or BF was not disturbed by ionic strength. Although a little higher adsorption removal rate of MGO@CP5 for MB (>99%) than BF (>96%) was noticed, it seemed to be innocuous. The reason might be that MGO@CP5 revealed the relatively high maximum uptake capacities toward

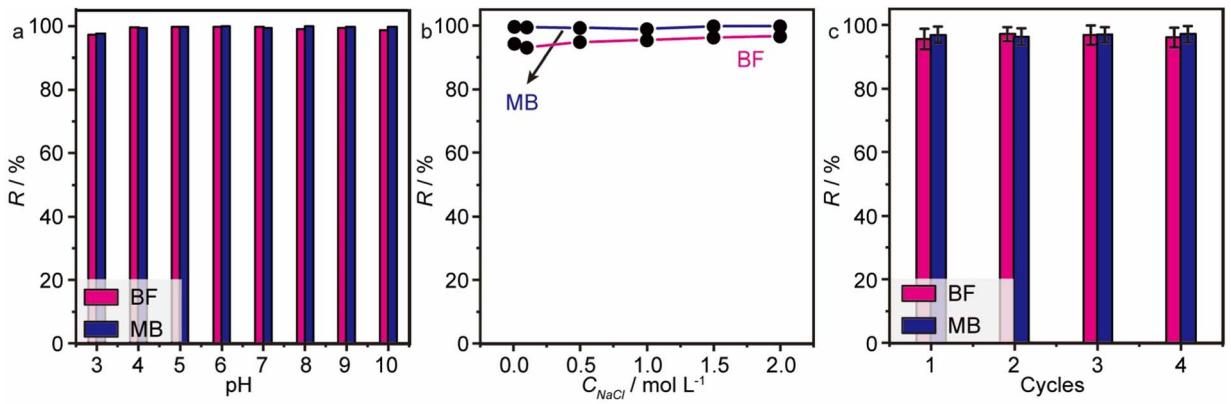

Fig. 6 The effect of pH (a) and ionic strength (b) on the adsorption of BF and MB on MGO@CP5. (c) The recycling performance of MGO@CP5 in the removal of BF and MB.

MB in contrast to BF; thus, the removal rate of MB exceeded the value of BF when the initial concentration of the two dyes was the same. The above results reflected that MGO@CP5 was capable of resisting interference from ion strength, further enhancing the possibilities in practical adsorption application.

Desorption and recyclability

To better evaluate the prospect of MGO@CP5 in real circumstances, its adsorption recycling performances toward BF and MB were further tested in model wastewater. The adsorption-saturated adsorbents were regenerated by ethanol elution containing 0.01 M HCl solution ($V_{EtOH} : V_{HCl} = 8 : 1$). In Fig. 6c, the removal efficiencies of BF and MB toward cycling numbers of MGO@CP5 are presented, where a slight decline in absorption efficiency but a high removal rate over 95% for cationic dyes after 4 cycles can be distinctly noticed, which testifies the good recyclability and great adsorption behavior of MGO@CP5.

Adsorption mechanism

For deeply confirming the adsorption pattern and fully exploring the adsorption mechanism, the FT-IR spectra of MGO@CP5 before and after adsorption as well as the spectra of the adsorbates were measured (Fig. 7a and b). Compared with initial MGO@CP5, the characteristic peak at about 3421 cm^{-1}, representing the stretching vibration of O–H, noticeably shifted to 3430 cm^{-1} and 3436 cm^{-1} after BF and MB adsorption, respectively, implying that phenolic hydroxyl might play a significant role during the adsorption process. The peak centered at about 1730 cm^{-1}, corresponding to the stretching vibration of carboxylate groups, shifted to other positions of 1736 cm^{-1} and 1738 cm^{-1} after BF and MB adsorption, respectively, thus confirming the importance of carboxyl groups on MGO@CP5 in the adsorption of BF and MB. Furthermore, the typical adsorption band at 1576 cm^{-1} belonging to aromatic rings also revealed the shift to 1583 cm^{-1} and 1594 cm^{-1} when BF and MB were absorbed by MGO@CP5. These changes could demonstrate the possible formation of hydrogen bonds and π–π stacking interaction as well as host–guest interaction between the adsorbent and the dyes.

Apart from this, the zeta potentials before and after adsorption were also obtained to determine the charge changes of MGO@CP5 and MGO@CP5–dye. The observation that the surface charge differences were apparent with and without the loading of BF and MB on MGO@CP5 was made, as presented in Fig. 7c. For the materials of absorbed cationic model dyes, namely, the surface charge of MGO@CP5–BF and MGO@CP5–MB became relatively less negative, representing the successful capture of BF and MB on MGO@CP5.

Overall, in view of the above-mentioned results, the adsorption mechanism might involve the formation of hydrogen bonds and π–π stacking interaction, the occurrence of electrostatic interaction, and host–guest interaction between the MGO@CP5 and dyes.

Adsorption of mixture dyes

Considering practical application demands, the selective adsorption of cationic dyes from MGO@CP5 was further investigated in a mixed aqueous solutions containing several cationic and anionic dyes. Herein, MO was selected as an anionic dye model, while BF and MB were chosen as the cationic dye model, and the structures of the three types of dyes are displayed in Fig. S7.† Besides, Fig. S8† describes the UV-vis absorption spectra variations and color changes of independent BF, MB, and MO solution. It was noteworthy that a significantly reduced UV-vis absorption intensity and almost colorless solution could be observed through the adsorption of BF and MB by MGO@CP5, evidencing that the dye concentration was sharply decreased after being adsorbed *via* electrostatic interaction and host–guest interaction. Nevertheless, the color (orange) and UV-vis spectra of MO were nearly unchanged through the adsorption process. These indicated that MGO@CP5 possessed the potential for selectively adsorbing cationic dyes. Further, MGO@CP5 was used to treat the cationic and anionic dyes' mixture solution. The visible observations were that the orange (inset of Fig. 8a) of BF/MO and green (inset of Fig. 8b) of MB/MO in the binary mixture solution gradually turned yellow. It was not hard to infer that the color change of the solution possibly accounted for the complete removal of BF or MB by MGO@CP5

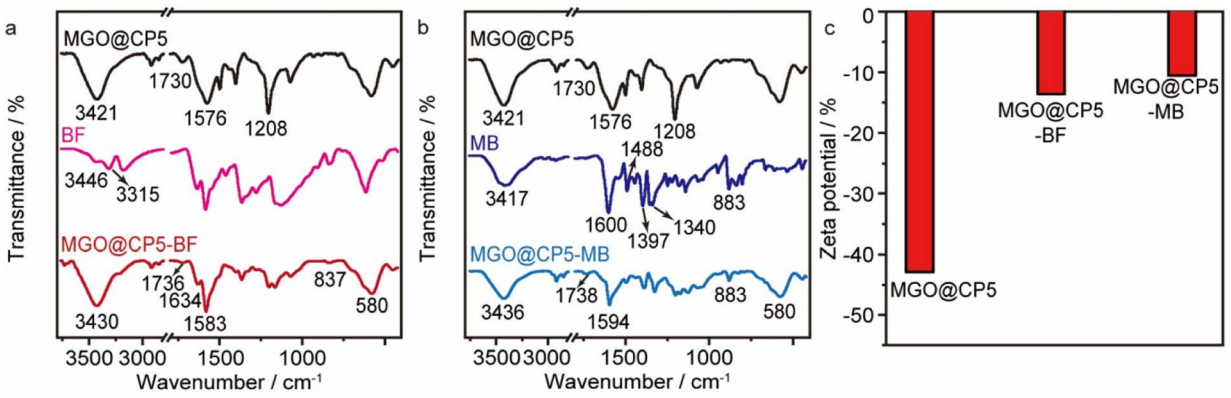

Fig. 7 The FT-IR spectra of MGO@CP5 before and after BF (a) and MB (b) adsorption. (c) The zeta potential (pH = 7) of MGO@CP5 before and after BF and MB adsorption.

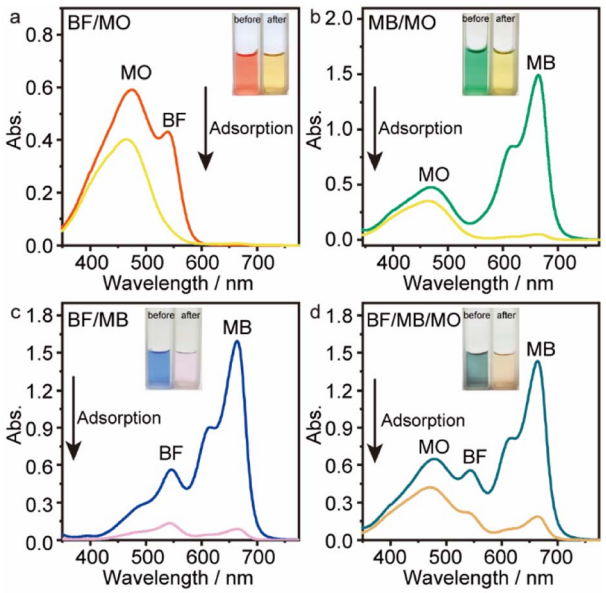

Fig. 8 The UV-vis adsorption spectra of (a) 3.0 mg L^{-1} BF and 3.3 mg L^{-1} MO mixed binary solution, (b) 3.2 mg L^{-1} MB and 3.3 mg L^{-1} MO mixed binary solution, (c) 3.0 mg L^{-1} BF and 3.2 mg L^{-1} MB mixed binary solution, (d) 3.0 mg L^{-1} BF, 3.3 mg L^{-1} MO, and 3.2 mg L^{-1} MB mixed ternary solution before and after adsorption by MGO@CP5. Inset: the pictures before (left) and after (right) the adsorption of mixed binary (BF/MO, MB/MO, and BF/MB) or ternary solution (BF/MO/MB) on MGO@CP5.

and the existence of only MO in the solution. Actually, the corresponding adsorption peak of BF (540 nm) and MB (668 nm) approximately disappeared after adsorption, while the intensity peaked at 464 nm, belonging to MO, exhibited a negligible decrease in the UV-vis spectra (Fig. 8a and b). For the mixed solution of cationic dyes BF/MB, the maximum adsorption peak of BF and MB significantly decreased after adsorption by MGO@CP5 (Fig. 8c). Correspondingly, the ternary dye system of the mixed BF/MO/MB was also measured and further demonstrated the sharply and largely weakening of the dyes of BF and MB but only the inconspicuous variation of the signal of MO after adsorption (Fig. 8d). The above phenomena reflected that MGO@CP5 was effective in the adsorption and selective removal of cationic dyes from aqueous solution, thereby confirming its great prospect as a superior adsorbent for dye removal and purification in wastewater treatment.

Conclusion

The magnetic adsorbent MGO@CP5 with excellent adsorption capacity for cationic dyes was facilely synthesized by carrying CP5 with supramolecular recognition on the surface of MGO, which possesses magnetic property. MGO@CP5 could adsorb 99% BF and MB within 3 minutes, and the maximum adsorption capacity can reach 132 mg g^{-1} for BF or 240 mg g^{-1} MB under optimal adsorption conditions. Furthermore, the adsorption kinetics results and the isotherm experimental data could relatively comply with the pseudo-second-order kinetics and Langmuir adsorption isotherm for adsorption process, respectively, implying that chemisorption due to the electrostatic interaction and monolayer adsorption played leading roles in the adsorption process. Sensibly, the adsorption behaviors of MGO@CP5 for BF and MB demonstrated a strong resistance toward pH changes and ionic strength. In addition, MGO@CP5 exhibited an excellent recycling behavior for cationic dyes with the removal efficiencies larger than 95% after recycling four times. This research manifested that MGO@CP5 had specific selective adsorption performance and high removal efficiency for cationic dyes, which is supposed to be a promising and stable adsorbent for the treatment of cationic dyes in water.

Conflicts of interest

There are no conflicts to declare.

Acknowledgements

This work was supported by the National Natural Science Foundation of China (No. 21976113), Research Project Supported by Shanxi Scholarship Council of China (No. 2021-009), Special Funds of S&T Cooperation and Exchange Projects of Shanxi Province (202204041101040), the Hundred Talent Program of Shanxi Province and the Natural Science Foundation of Zhejiang Province (No. LY22B040001).

References

1 T. Liu, C. O. Aniagor, M. I. Ejimofor, M. C. Menkiti, Y. M. Wakawa, J. Li, R. A. Akbour, P. S. Yap, S. Y. Lau and J. Jeevanandam, *J. Ind. Eng. Chem.*, 2023, **117**, 21–37.
2 X. Ji, H. Wang, H. Wang, T. Zhao, Z. A. Page, N. M. Khashab and J. L. Sessler, *Angew. Chem., Int. Ed.*, 2020, **59**, 23402–23412.
3 Y. Gao, S. Q. Deng, X. Jin, S. L. Cai, S. R. Zheng and W. G. Zhang, *Chem. Eng. J.*, 2019, **357**, 129–139.
4 H. Ouachtak, A. E. Guerdaoui, R. E. Haouti, R. Haounati, H. Ighnih, Y. Toubi, F. Alakhras, R. Rehman, N. Hafid, A. A. Addi and M. L. Taha, *RSC Adv.*, 2023, **13**, 5027–5044.
5 J. Ding, H. J. Khan, G. Vahedi Sarrigani, P. Fitzgerald, A. Ebrahimi Ghadi, O. Lefebvre, C. Meng, M. H. Z. Mohd Harun, Y. Lu, A. Abbas, A. Montoya, D. Wiley and D. K. Wang, *Chem. Eng. J.*, 2022, **432**, 134435–134443.
6 R. Gurav, S. K. Bhatia, T. R. Choi, Y. K. Choi, H. J. Kim, H. S. Song, S. M. Lee, S. Lee Park, H. S. Lee, J. Koh, J. M. Jeon, J. J. Yoon and Y. H. Yang, *Chemosphere*, 2021, **264**, 128539–128540.
7 E. Saputra, B. A. Prawiranegara, M. W. Nugraha, N. S. Sambudi, H. Sugesti, A. Awaluddin, Komalasari, P. S. Utama and M. Manawan, *Environ. Sci. Pollut. Res.*, 2023, **30**, 39961–39977.
8 C. C. Cheng, T. W. Chiu, X. J. Yang, S. Y. Huang, W. L. Fan, J. Y. Lai and D. J. Lee, *Polym. Chem.*, 2019, **10**, 827–834.
9 F. Zhao, E. Repo, D. Yin, Y. Meng, S. Jafari and M. Sillanpaa, *Environ. Sci. Technol.*, 2015, **49**, 10570–10580.

10 G. Xu, X. Xie, L. Qin, X. Hu, D. Zhang, J. Xu, D. Li, X. Ji, Y. Huang, Y. Tu, L. Jiang and D. Wei, *Green Chem.*, 2019, **21**, 6062–6072.
11 Y. Rong, Y. Huang, P. Jin, C. Yang, Z. Zhong, C. Dong and W. Liang, *J. Water Proc. Eng.*, 2020, **37**, 101345–101356.
12 M. K. K. Kadirvelu, C. Karthika, M. Radhika, N. Vennilamani and S. Pattabhi, *Bioresour. Technol.*, 2003, **87**, 129–132.
13 G. V. Briao, S. L. Jahn, E. L. Foletto and G. L. Dotto, *J. Colloid Interface Sci.*, 2017, **508**, 313–322.
14 Y. Qi, M. Yang, W. Xu, S. He and Y. Men, *J. Colloid Interface Sci.*, 2017, **486**, 84–96.
15 H. Chen, Q. Gao, J. Li and J. M. Lin, *J. Photochem. Photobiol., C*, 2016, **27**, 54–71.
16 W. Liang, Y. Huang, D. Lu, X. Ma, T. Gong, X. Cui, B. Yu, C. Yang, C. Dong and S. Shuang, *Polymers*, 2019, **11**, 133–148.
17 C. Wen, R. Cheng, T. Gong, Y. Huang, D. Li, X. Zhao, B. Yu, D. Su, Z. Song and W. Liang, *Colloids Surf., B*, 2021, **199**, 111510–111520.
18 W. Liu, Y. An, L. Wang, T. Hu, C. Li, Y. Xu, K. Wang, X. Sun, H. Zhang, X. Zhang and Y. Ma, *J. Energy Chem.*, 2023, **80**, 68–76.
19 Z. Jing, Y. Li, Y. Zhang, K. Chen, Y. Sun, M. Wang, B. Chen, S. Zhao, Y. Jin, Q. Du, X. Pi and Y. Wang, *Int. J. Biol. Macromol.*, 2023, **242**, 124683–124697.
20 W. J. D. Nascimento Júnior, G. H. D. Aguiar, R. Landers, M. G. A. Vieira and M. A. D. Motta Sobrinho, *Colloids Surf., A*, 2023, **671**, 131647–131653.
21 A. Kakanakova-Georgieva, I. G. Ivanov, N. Suwannaharn, C.-W. Hsu, I. Cora, B. Pécz, F. Giannazzo, D. G. Sangiovanni and G. K. Gueorguiev, *CrystEngComm*, 2021, **23**, 385–390.
22 D. G. Sangiovanni, R. Faccio, G. K. Gueorguiev and A. Kakanakova-Georgieva, *Phys. Chem. Chem. Phys.*, 2023, **25**, 829–837.
23 T. Ullah, K. Gul, H. Khan, B. Ara and T. U. H. Zia, *Chemosphere*, 2022, **293**, 133452–133461.
24 C. Bo, Z. Jia, B. Liu, X. Dai, G. Ma and Y. Li, *J. Taiwan Inst. Chem. Eng.*, 2022, **138**, 104499–104511.
25 H. R. Nodeh, M. A. Kamboh, W. A. Wan Ibrahim, B. H. Jume, H. Sereshti and M. M. Sanagi, *Environ. Sci.: Processes Impacts*, 2019, **21**, 714–726.
26 Y. Liu, C. Luo, G. Cui and S. Yan, *RSC Adv.*, 2015, **5**, 54156–54164.
27 H. Wang and Y. Wei, *RSC Adv.*, 2017, **7**, 9079–9089.
28 K. Li, J. Yan, Y. Zhou, B. Li and X. Li, *J. Mol. Liq.*, 2021, **335**, 116291–116310.
29 M. Y. Qi, M. Conte, M. Anpo, Z. R. Tang and Y. J. Xu, *Chem. Rev.*, 2021, **21**, 13051–13085.
30 S. Lan, S. Zhan, J. Ding, J. Ma and D. Ma, *J. Mater. Chem. A*, 2017, **5**, 2514–2518.
31 B. Shi, H. Guan, L. Shangguan, H. Wang, D. Xia, X. Kong and F. Huang, *J. Mater. Chem. A*, 2017, **5**, 24217–24222.
32 T. Ogoshi, T. A. Yamagishi and Y. Nakamoto, *Chem. Rev.*, 2016, **116**, 7937–8002.
33 L. Li, R. Chen, T. Hu, Y. Li, Q. Wang and C. He, *Microchem. J.*, 2020, **153**, 104524–104530.
34 H. Zhang, J. R. Wu, X. Wang, X. S. Li, M. X. Wu, F. Liang and Y. W. Yang, *Dyes Pigm.*, 2019, **162**, 512–516.
35 W. Liang, Y. Rong, L. Fan, W. Dong, Q. Dong, C. Yang, Z. Zhong, C. Dong, S. Shuang and W. Y. Wong, *J. Mater. Chem. C*, 2018, **6**, 12822–12829.
36 D. C. Marcano, J. M. Berlin, A. Sinitskii, Z. Z. Sun, A. Slesarev, L. B. Alemany, W. Lu and J. M. Tour, *ACS Nano*, 2010, **4**, 4806–4814.
37 S. K. T. Ogoshi, S. Fujinami, T. A. Yamagishi and Y. Nakamoto, *J. Am. Chem. Soc.*, 2008, **130**, 5022–5023.
38 T. Ogoshi, M. Hashizume, T. A. Yamagishi and Y. Nakamoto, *Chem. Commun.*, 2010, **46**, 3708–3710.
39 X. Duan, Z. Ao, H. Sun, S. Indrawirawan, Y. Wang, J. Kang, F. Liang, Z. H. Zhu and S. Wang, *ACS Appl. Mater. Interfaces*, 2015, **7**, 4169–4178.